2018

Solid-state synapse based on magnetoelectrically coupled memristor

Weichuan Huang, Yue-Wen Fang, Yuewei Yin, Bobo Tian, Wenbo Zhao, Chuangming Hou, Chao Ma, Qi Li, Evgeny Y. Tsymbal, Chun-Gang Duan, and Xiaoguang Li

ACS APPLIED MATERIALS & INTERFACES

Research Article

Cite This: ACS Appl. Mater. Interfaces 2018, 10, 5649−5656

www.acsami.org

Solid-State Synapse Based on Magnetoelectrically Coupled Memristor

Weichuan Huang,[†] Yue-Wen Fang,[‡] Yuewei Yin,[*,†,§] Bobo Tian,[‡] Wenbo Zhao,[†] Chuangming Hou,[†] Chao Ma,[†] Qi Li,[‖] Evgeny Y. Tsymbal,[§] Chun-Gang Duan,[*,‡,⊥] and Xiaoguang Li[*,†,#]

[†]Hefei National Laboratory for Physical Sciences at the Microscale, Department of Physics, University of Science and Technology of China, Hefei 230026, China

[‡]Key Laboratory of Polar Materials and Devices, Ministry of Education, Department of Electronic Engineering, East China Normal University, Shanghai 200241, China

[§]Department of Physics and Astronomy, University of Nebraska, Lincoln, Nebraska 68588, United States

[‖]Department of Physics, Pennsylvania State University, University Park 16802, United States

[⊥]Collaborative Innovation Center of Extreme Optics, Shanxi University, Shanxi 030006, China

[#]Collaborative Innovation Center of Advanced Microstructures, Nanjing 210093, China

Supporting Information

ABSTRACT: Brain-inspired computing architectures attempt to emulate the computations performed in the neurons and the synapses in the human brain. Memristors with continuously tunable resistances are ideal building blocks for artificial synapses. Through investigating the memristor behaviors in a $La_{0.7}Sr_{0.3}MnO_3/BaTiO_3/La_{0.7}Sr_{0.3}MnO_3$ multiferroic tunnel junction, it was found that the ferroelectric domain dynamics characteristics are influenced by the relative magnetization alignment of the electrodes, and the interfacial spin polarization is manipulated continuously by ferroelectric domain reversal, enriching our understanding of the magnetoelectric coupling fundamentally. This creates a functionality that not only the resistance of the memristor but also the synaptic plasticity form can be further manipulated, as demonstrated by the spike-timing-dependent plasticity investigations. Density functional theory calculations are carried out to describe the obtained magnetoelectric coupling, which is probably related to the Mn−Ti intermixing at the interfaces. The multiple and controllable plasticity characteristic in a single artificial synapse, to resemble the synaptic morphological alteration property in a biological synapse, will be conducive to the development of artificial intelligence.

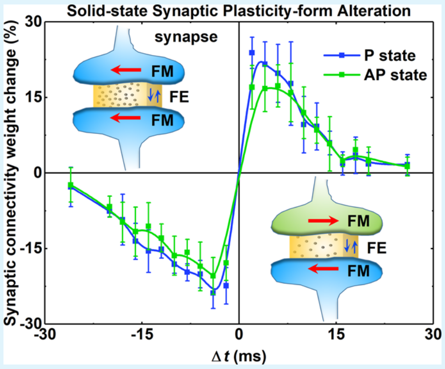

KEYWORDS: *multiferroic tunnel junctions, magnetoelectric coupling, interface, memristor, synaptic plasticity*

1. INTRODUCTION

The information in the human brain is transmitted, stored, and processed in the neuron network through synapses. Synapses capable of varying their connecting strength due to the change of their activity, the so-called synaptic plasticity, play a fundamental role in the abilities of learning and memory.[1−3] The new emerging memristor with a continuously tunable resistance can be treated as an electronic equivalent of the synapse for artificial neural networks.[4,5] The memristor was first demonstrated experimentally in titanium oxide capacitors where continuous resistance states involve coupled motion of electrons and ions within the oxide layer under an applied electric field.[6] Since then, to further improve the efficiency of emulating synapses, considerable efforts have been dedicated to investigating memristors based on different mechanisms, including spintronic,[7,8] ferroelectric,[9−11] phase-change,[12,13] ionic/electronic hybrid or 2D material three-terminal memristors,[14,15] and so forth. Magnetic tunnel junctions (MTJs) are typical spintronic memristors, where the multilevel resistances are linked to the continuous displacement of the magnetic domain walls (DWs).[7,8] However, the resistance and tunneling magnetoresistance (TMR) variations in most MTJ-based memristors are not quasicontinuous and produced by a high operating current density of 10^6 to 10^7 A/cm^2.[7,8,16] On the other hand, ferroelectric tunnel junctions (FTJs) have been demonstrated to be good candidates for low energy consumption memory devices with high performance.[17,18] It is known that the resistance states in FTJ-based memristors can be continuously tuned by engineering the ferroelectric domain states associated with the ferroelectric domain nucleation and growth dynamics.[9,10] The plasticity of conductance in these memristors confirms their potential for emulating the plasticity,

Received: November 30, 2017
Accepted: January 25, 2018
Published: January 25, 2018

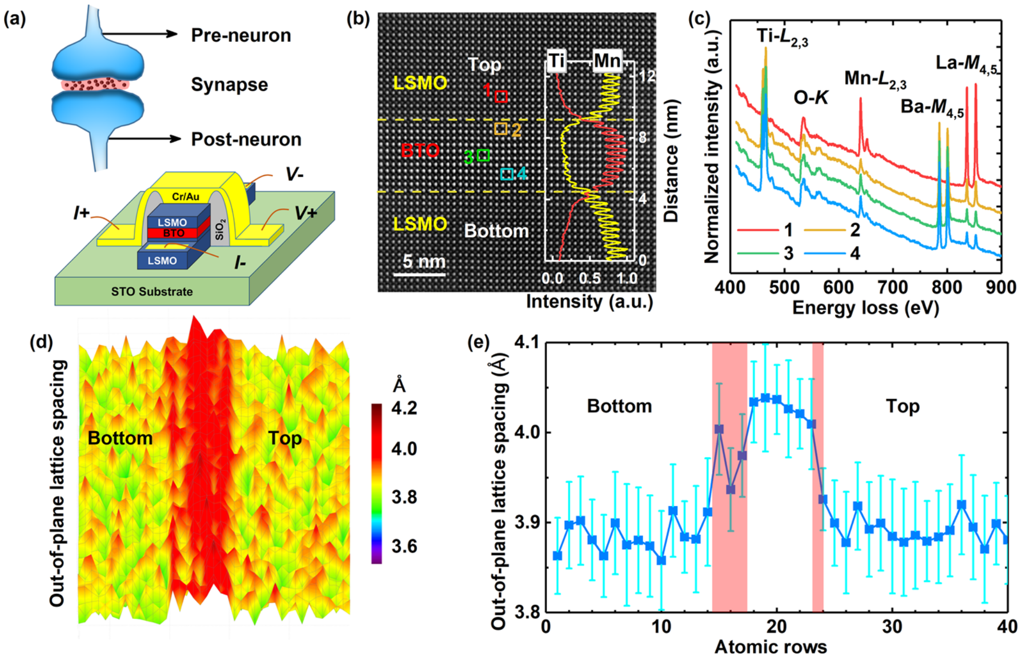

Figure 1. (a) Sketch of preneurons and postneurons connected by a synapse, and the magnetoelectrically coupled memristor based on LSMO/BTO/LSMO MFTJ. (b) STEM−HAADF image of the LSMO/BTO/LSMO trilayer. Inset: Elemental profiles of Ti and Mn. (c) EELS spectra acquired at different positions as illustrated in the HAADF image in (b). (d,e) Bird's eye map and the mean value of the out-of-plane lattice spacing, respectively. The blue shaded areas in (e) indicate the width of both LSMO/BTO interfaces.

particularly spike-timing-dependent plasticity (STDP), of biological synapses and thus learning and memory abilities.[9] However, these memristor prototypes only show a single plasticity form in one device unit cell. While it is believed that in biological synapses, synaptic morphological alterations (including synaptic density, curvature, perforations, and the size of synaptic elements) will result in different forms of synaptic plasticity.[19] The multiple plasticity forms in analogous to the property of multimorphology in a single biological synapse has not been achieved in any memristor device above, limiting its complete emulation of natural synapses in human brains.

Artificial multiferroic tunnel junctions (MFTJs), employing ferroelectric barriers in MTJs or ferromagnetic electrodes in FTJs, provide not only the combined functionalities of MTJs and FTJs to achieve multistate devices[20−24] but also promising applications utilizing the magnetoelectric coupling at the ferromagnetic/ferroelectric interfaces.[25−28] The interfacial spin polarization and the TMR can be tuned via ferroelectric polarization reversal.[26−28] Using an MFTJ as a memristor, one can manipulate the resistance by modifying not only magnetic states but also ferroelectric domains, which enhances the operability in the plasticity of artificial synapses based on MFTJs. Furthermore, from the point of view of magnetoelectric coupling,[29] it could be expected that for a memristor based on MFTJs, the magnetic states of electrodes may affect the ferroelectric memristive behaviors, which can provide a way to emulate the property of different biological synaptic morphologies. However, this has not been discovered yet. Meanwhile, it will be interesting to investigate whether the TMR-based memristive behavior can be tuned by energy efficient ferroelectric control.

Here, by investigating the voltage-controlled resistance variations in $La_{0.7}Sr_{0.3}MnO_3/BaTiO_3/La_{0.7}Sr_{0.3}MnO_3$ (LSMO/BTO/LSMO) MFTJs, we found that the interfacial spin configuration can modify the ferroelectric memristive dynamics and that the interfacial spin polarization can be continuously manipulated by electric field. Density functional theory calculations allow us to understand the effect of magnetic states on the ferroelectric switching behaviors. Such an individual electronic solid-state synapse, which can capture diversified plasticity forms, can bring another degree of freedom to the design of complex cognitive systems of artificial intelligence in the future.

2. RESULTS AND DISCUSSION

2.1. Atomic Structures at the Interfaces. To emulate a biological synapse, we work with an electronic memristor based on LSMO/BTO/LSMO MFTJs, as sketched in Figure 1a. Figure 1b shows an aberration-corrected high-angle annular dark-field (HAADF) scanning transmission electron microscopy (STEM) images and core-level electron energy-loss spectroscopy (EELS) line scans of an LSMO/BTO/LSMO trilayer, demonstrating the single crystalline, fully epitaxial BTO and LSMO. The thickness of the BTO barrier is approximately 9 unit cells. Furthermore, we acquired the EELS spectra at different positions of the trilayer, as shown in Figure 1c. Referring to the signal of Mn-$L_{2,3}$ at the LSMO electrode (spectrum 1 shown in Figure 1c), the weak signal of Mn-$L_{2,3}$ can be detected inside of the BTO barrier (spectra 2−4), indicating the small amount of Mn ions inside of the BTO barrier.

By using the quantitative analysis of the atomic-resolution HAADF−STEM image (the probe scanning direction is along the growth direction), the two-dimensional atom positions could be confirmed by 2D Gaussian fitting and the structural parameters for each unit cell can be obtained. The spatial distribution of the out-of-plane lattice spacing is displayed in Figure 1d,e. The out-of-plane lattice spacing increases abruptly at the BTO/LSMO top interface (Figure 1e), indicating an

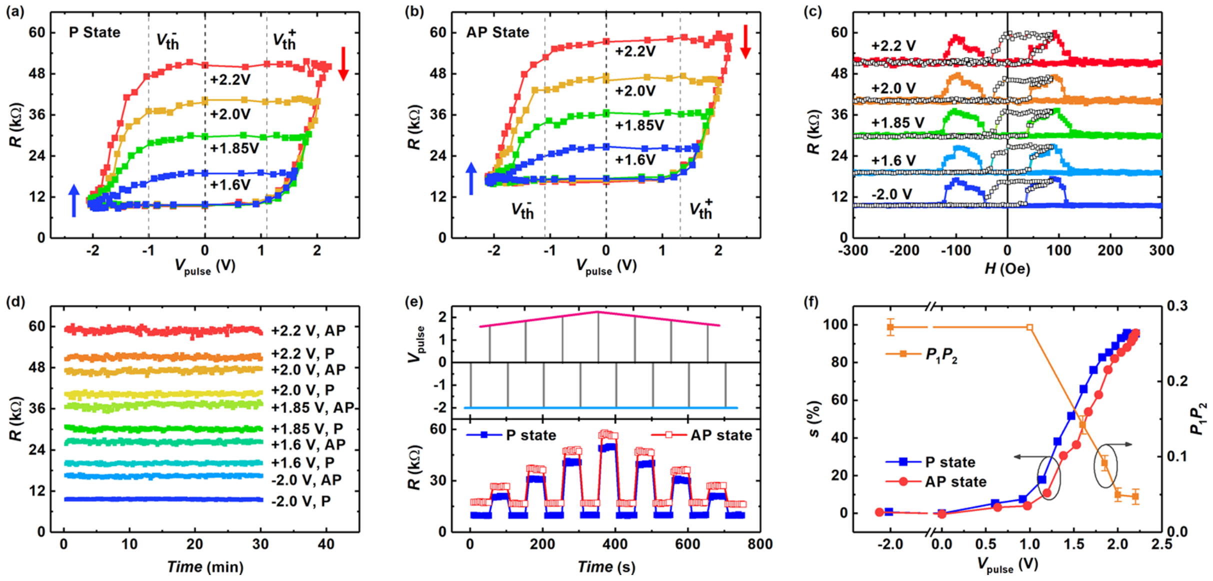

Figure 2. Junction resistances recorded at 10 mV as a function of voltage pulses with the positive maximum voltage increasing from 1.6 to 2.2 V for (a) parallel magnetic state and (b) antiparallel magnetic state, respectively. The dash lines show the voltage thresholds (V_{th}^{+} and V_{th}^{-}) and the single-headed arrows show the directions of ferroelectric polarization. (c) Junction resistances recorded at 10 mV as a function of magnetic fields after different voltage pulses. Solid square: typical R−H curves. Open circles: resistance memory loops showing nonvolatile resistance states. (d) Data retention of the MFTJ at 10 different states up to 30 min. (e) Reversibility test of switching among multistates using sequence of voltage pulses: (top) the applied voltage pulses and (bottom) response of resistance. (f) Voltage pulse dependences of s estimated by resistance for P and AP states and the effective interfacial spin polarization of the MFTJ.

atomically sharp interface. In contrast, the LSMO/BTO bottom interface is more gradual, consistent with our previous result that there are more Mn−Ti intermixing at the bottom interface than that at the top interface.[24]

2.2. Magnetoelectrically Coupled Memristor Behaviors.

The memristive behaviors were performed by measuring the pulsed voltage (V_{pulse}, 100 ms) dependent resistances (R) for parallel (P) and antiparallel (AP) magnetic states, as shown in Figure 2a,b. The P and AP magnetic states were confirmed and realized at zero magnetic field (H) by measuring R−H curves, as shown in Figure 2c. The junction resistance (at 10 mV) versus V_{pulse} hysteresis loops were measured with V_{pulse} swept in the −2.0 V → +V_{max} → −2.0 V sequence, where V_{max} increased from 1.6 to 2.2 V. The MFTJ was set to low-resistance states by negative voltage pulses and to high-resistance states by positive voltage pulses. Here, the variation of the junction resistance is directly linked to the different ferroelectric status in the $BaTiO_3$ barrier in which the robust ferroelectricity is evidenced by piezoresponse force microscopy (see Supporting Information Figure S1). We define the low resistances after V_{pulse} = −2.0 V as on states (upward ferroelectric polarization) and the high resistances after V_{pulse} = +2.2 V as off states (downward ferroelectric polarization). Interestingly, the resistance switching between the on state and the off state shows a broad range of intermediate resistance states. Different intermediate resistance states can be achieved nonvolatilely by tuning the magnitude of V_{pulse}, which clearly demonstrates a memristive behavior. Treating the continuously tunable resistance as the biological synaptic strength, a low (high) resistance is regarded analogous to a strong (weak) synaptic connection.[4,9] Thus, in the implementation of artificial synapses for our memristors, the decrease/increase in junction resistances after negative/positive voltage pulses can be used to emulate the potentiation/depression of synaptic strength, respectively. It is noted that the R−V_{pulse} curves shift to the positive voltage side with the positive voltage thresholds (V_{th}^{+}) larger than the negative ones (V_{th}^{-}), as guided by the dash lines in Figure 2a,b. Here, the voltage thresholds V_{th}^{+} (or V_{th}^{-}) are defined as the ones where the resistances are 10% higher (or lower) than those at on (or off) states. In addition, both V_{th}^{+} and V_{th}^{-} for the P magnetic state are lower than those for the AP magnetic state, indicating different memristive behaviors between P and AP magnetic states. Furthermore, to demonstrate its potential in high density memories as expected in memristors,[30] we applied −2.0 V → +V_{max} write pulses with different +V_{max} (1.6, 1.85, 2, and 2.2 V) to set junctions into different polarization states. Combining the TMR effect, 10 distinguishable nonvolatile, stable, and reversible states were obtained, as shown in Figure 2d,e.

The memristive behaviors can be analyzed using the voltage-controlled ferroelectric-domain nucleation and growth model. Defining s as the relative area fraction of the ferroelectric down domains, the on and off states can be treated as fully ferroelectric up (s = 0) and down (s = 1) states, while the intermediate state is a mixture of regions with ferroelectric up and down states (0 < s < 1). Thus, the s for any intermediate state could be extracted from its resistance according to a parallel circuit model[9,10]

$$\frac{1}{R} = \frac{1 - s}{R_{on}} + \frac{s}{R_{off}} \tag{1}$$

where R_{on} and R_{off} represent the junction resistances of on and off states at the P or AP magnetic state, respectively. Figure 2f shows the relative fraction s during the R−V_{pulse} scans for P and AP magnetic states. It shows that with increasing positive voltage pulse magnitude, s varies from 0 in the on state to 1 in the off state. Importantly, after a same positive voltage pulse from the on to off states, the s for the P magnetic state is larger than that for the AP magnetic state, which means the memristive manipulation associated with the ferroelectric

DOI: 10.1021/acsami.7b18206
ACS Appl. Mater. Interfaces 2018, 10, 5649−5656

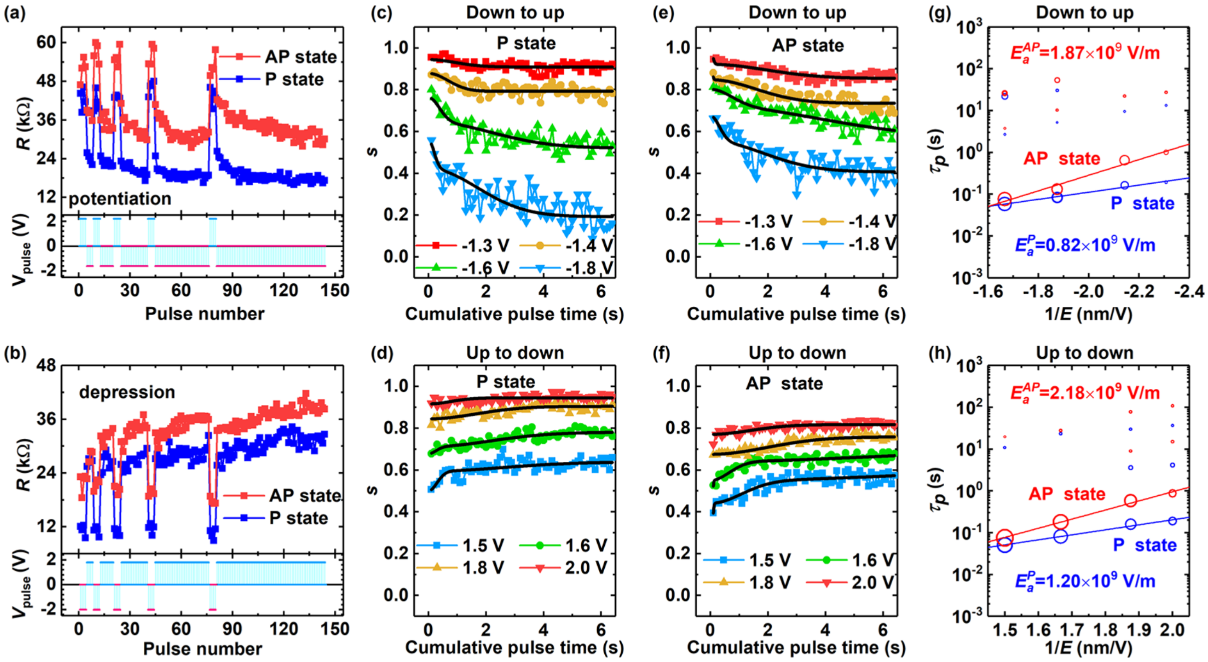

Figure 3. Evolution of the junction resistances for P and AP states upon voltage pulse sequences of (a) V_{pulse} = +2.2 and −1.6 V with a duration of 100 ms, and (b) V_{pulse} = −2 and +1.8 V with a duration of 100 ms. The cumulative pulse time dependences of the switched fraction for down-to-up (c,e) and up-to-down (d,f) switchings with different voltage amplitudes at P and AP states. The lines are the fits using eqs 2 and 3. Propagation time vs $1/E$ of the different zones for (g) down-to-up and (h) up-to-down switchings. The symbol size is proportional to the corresponding size of the considered zone, and the solid lines are fits based on Merz's law.

domain switching is easier at the P magnetic state. The difference of ferroelectric memristive behaviors between P and AP magnetic states confirms the potential of such a magnetoelectrically coupled memristor for emulating the synapses with diversified plasticity characteristics. Just like the ferroelectric property can be affected by the magnetic state, the magnetic property, e.g., TMR effect, can also be tuned by ferroelectric reversal. As shown in Figure 2c, the TMR value at the on state is ~75% (defined as TMR = $(R_{\text{AP}} - R_{\text{P}})/R_{\text{P}}$, where R_{P} and R_{AP} are the resistances in the parallel and antiparallel states, respectively), and it gradually decreases to ~10% with an increasing positive pulse amplitude to +2.2 V. Correspondingly, large and tunable tunnel electromagnetoresistance values suggesting interfacial magnetoelectric coupling are obtained as shown in Supporting Information Figure S2. According to the Julliere model,[31] TMR = $2P_1P_2/(1 - P_1P_2)$, TMR is related to the effective spin polarizations P_1 and P_2 at the top and bottom ferromagnetic/ferroelectric interfaces. The variations of the TMR with the ferroelectric polarization reflect the changes in spin polarization upon the ferroelectric polarization. Thus, we can estimate P_1P_2 versus pulse voltages, as shown in Figure 2f. It is found that P_1P_2 of ~0.27 after a negative pulse voltage of −2.0 V (ferroelectric poled up) gradually reduces upon pulse voltage reversal and down to ~0.047 after a positive pulse voltage of +2.2 V (ferroelectric poled down). The continuous manipulation in the effective spin polarization demonstrates a way to achieve the TMR-based memristive behavior by the gradual ferroelectric reversal. This is another function in magnetoelectrically coupled MFTJ-based memristor and is more power-efficient than the simple MTJ-based memristors.[16] Furthermore, the continuously tunable spin polarization is a desired functionality for spintronics technology.

2.3. Magnetoelectrically Coupled Ferroelectric Domain Dynamics.

We now investigate the resistance evolutions upon voltage pulse numbers (durations). It has been reported that the velocity of the ferroelectric DW motion varies from 10^{-8} to 3000 m/s, depending on the amplitude and duration of the applied electric field,[32−34] and thus the time of DW motion in micrometer along the interface can be up to a few seconds.[34,35] Through repetitive application of voltage pulses (100 ms) of a certain polarity and amplitude, the junction resistances can be continuously tuned. As shown in Figure 3a, after applying four consecutive positive pulses with an amplitude of 2.2 V to set the junction into high-resistance states for both parallel and antiparallel states, the resistance continuously decreases (synaptic potentiation) with the increasing number of negative write pulses of −1.6 V. Vice versa, as shown in Figure 3b, beginning from a low resistance state set by four negative pulses (−2.0 V), the resistance increases continuously (synaptic depression) with the increasing number of positive write pulses of 1.8 V. Such resistance evolutions upon voltage pulse numbers are repeatable as shown in Supporting Information Figure S3.

After converting the resistances to ferroelectric domain ratios, Figure 3c−f show a typical set of data on the evolution of s as a function of cumulative pulse time (t). As proposed by Chanthbouala et al.,[10] the junction area can be divided into a finite number of zones N with different propagations ruled by the Kolmogorov−Avrami−Ishibashi model.[36,37] Considering that the timescale for nucleation is typically 1 ps to 1 ns,[38] the nucleation processes under a relatively longer voltage pulse duration (100 ms) could be neglected. Thus, s can be written as

$$s = 1 - \sum_{i=1}^{N(i)} S_i \cdot \{1 - \exp[-(t/\tau_{\text{p}}{}^{i})^2]\} \tag{2}$$

for down-to-up switching, and

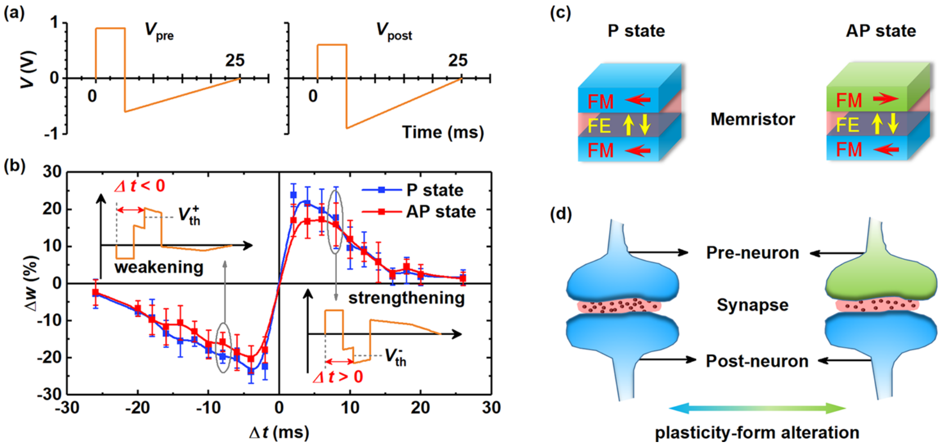

Figure 4. (a) Presynaptic and postsynaptic spikes with the total length of 25 ms. (b) Measurements of STDP in MFTJ with P and AP states. The insets show the waveforms produced by the superposition of presynaptic and postsynaptic spikes. (c) Schematic illustration of the magnetoelectrically coupled memristor and (d) Sketch of the corresponding synapses.

$$s = \sum_{i=1}^{N(i)} S_i \cdot \{1 - \exp[-(t/\tau_p^{\,i})^2]\} \tag{3}$$

for up-to-down switching, where S_i is the area of each zone normalized by the junction area and τ_p is a characteristic propagation time. Figure 3c,e (Figure 3d,f) shows the fits of the experimental data by eq 2 (eq 3) for negative (positive) voltage pulses with different amplitudes at the P and AP magnetic states. The data are well-fitted in the whole-time range with a reduced number of zones $N \leq 3$, see the solid lines in Figure 3c−f. The propagation time for each zone was extracted and plotted as a function of electric field (E) for negative (Figure 3g) and positive pulses (Figure 3h). The size of the symbol is proportional to the area S_i of the zone it represents.[10] It can be seen that, for all zones at each E, the values of τ_p at the AP magnetic state are larger than those at the P magnetic state.

Because the DW propagation is proportional to $\exp(-E_a/E)$ based on Merz's law,[39,40] we can obtain the activation electric field E_a by fitting the time versus $1/E$ data to further evaluate the difference of the resistance evolution behaviors between the parallel and antiparallel magnetic states. Here, we only consider the DW propagation of the largest zone at each E which dominates resistance variations at each voltage amplitude. The activation fields E_a for the DW propagations at the P magnetic state are 0.82×10^9 and 1.20×10^9 V/m for the down-to-up and the up-to-down domain switchings, respectively, while those at the AP magnetic state are 1.87×10^9 and 2.18×10^9 V/m for the down-to-up and the up-to-down domain switchings, respectively. These values of E_a are in the same order as reported by Boyn et al.[9] Importantly, the activation fields for the P magnetic state are always smaller than those for the AP magnetic state, which is consistent with the relatively easier ferroelectric switching upon voltage pulse for the P magnetic state as discussed above. This should be the reason why the resistance evolutions upon pulse numbers for the AP magnetic state are relatively slower than those for the parallel state.

2.4. Magnetoelectrically Coupled STDP.

To implement STDP in our MFTJs, we apply a voltage waveform shown in Figure 4a to our memristors to emulate the pre- and postneuron activities (V_{pre} and V_{post}). The voltage waveform is made up of rectangular voltage pulses followed by smooth slopes of opposite polarity, where the voltage never exceeds V_{th}, so that a single spike cannot induce a change in resistance. When both pre- and postneuron spikes reach the memristor with a delay Δt, their superposition produces the waveforms ($V_{pre} - V_{post}$) as displayed in the inset of Figure 4b (indicating the values of Δt in the figure), and the combined waveform transitorily exceeds the threshold voltage. As shown in Figure 4b, for a causal pre- to postspike timing relation ($\Delta t > 0$), the voltage activities will lead to the enhancement of the synaptic connectivity with a positive weight change (Δw, in percent), i.e., potentiation. While for an anticausal relation ($\Delta t < 0$), it results in the suppression of the synaptic connectivity, i.e., depression. Notably, as can be seen from the experimental STDP curves in Figure 4b, the change of the synaptic weight is larger for the P state than that for the AP state. This can be ascribed to the fact that the voltage thresholds of R−V_{pulse} curves or the activation fields for the P magnetic state are always smaller than those for the AP magnetic state, as discussed above. These results indicate that multiple and controllable STDP forms in a single artificial synapse based on MFTJ are realized, which is useful to mimic the property of morphological alterations in a biological synapse. More specifically, as sketched in Figure 4c,d, the memristor at the P magnetic state with relatively low resistances, small propagation time, and activation field corresponds to a relatively strong synaptic connection and a nonimpaired synaptic plasticity. While the memristor at the AP magnetic state with relatively high resistance, large propagation time, and activation field corresponds to a relatively weak synaptic connection and an impaired or declined synaptic plasticity. The changes of the magnetic states in such a magnetoelectrically coupled memristor from parallel to antiparallel are similar to the synaptic morphological alteration in a biological synapse, resulting in the variations of memory and learning abilities.[3,19,41] It is worth mentioning that the magnetic states in the MFTJ may be varied continuously as an MTJ,[8] which would lead to a continuously tunable plasticity form in this kind of solid-state synapse. Because integrating multiple plasticity forms in a single artificial synapse makes it more similar to a biological synapse, it may be particularly in demand for the integration of the magnetoelectrically coupled memristor based on MFTJs in the development of artificial intelligence.

2.5. First-Principles Calculations.

The ab initio plane-wave calculations were carried out to study the structural

DOI: 10.1021/acsami.7b18206
ACS Appl. Mater. Interfaces 2018, 10, 5649−5656

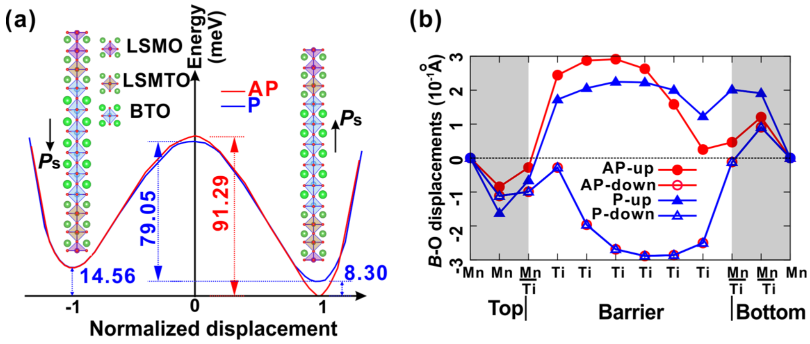

Figure 5. (a) Energy per slab model as a function of normalized displacement of soft mode distortion. The amplitude of the ion displacements along the *c*-axis is normalized, i.e., 1 and −1 correspond to the polarization (P_s) up and downward, respectively. The black single-headed arrows show the directions of ferroelectric polarization. The energy of polarization up in the AP magnetic state is taken as the reference energy. (b) Profile of the relative B−O (B = Ti, Mn, or Mn_mTi_{1-m}) displacements in each atomic layer in two polarization states under P and AP magnetic states.

properties of the MFTJ (see Methods). Here, considering the asymmetric Mn−Ti intermixing at the interfaces, the MFTJ was modeled by a structure in which a single monolayer (two monolayers) of $La_{0.7}Sr_{0.3}Mn_{0.5}Ti_{0.5}O_3$ separates the top (bottom) LSMO electrode from the BTO barrier film. The fully relaxed structures with polarization upward and downward states are shown in the insets of Figure 5a. The notable Ti−O displacements can be obtained directly from the relaxed structures, and their specific quantities are reported in Figure 5b. These results indicate that the nanoscale ferroelectricity survives in BTO sandwiched between the electrodes. We calculated the energy per supercell as a function of the soft mode distortion, as shown in Figure 5a. Two inequivalent energy minima in the curve are shown as the signature of asymmetric ferroelectricity in the MFTJs at P and AP magnetic states. The relative lower energy for polarization up indicates the BTO thin film energetically favors upward polarization, which is responsible for the shift of $R-V_{\text{pulse}}$ curves to the positive side in Figure 2a,b. Furthermore, we found that the ferroelectric polarization switching barrier for the AP magnetic state of ~91 meV/supercell is larger than that for the P magnetic state of ~79 meV/supercell, which indicates the ferroelectric polarization for the P magnetic state would be switched easier than that for the AP magnetic state. This computational result is in good agreement with the smaller activation field E_a for the P magnetic state compared with that for the AP magnetic state as obtained above. Note that the magnetic moments at Ti sites can be induced by the superexchange between Ti and Mn via the intermediate oxygen ions, the possibility of interlayer exchange coupling would be existing as a result.[42,43] This makes the B−O (B = Ti, Mn, or Mn_mTi_{1-m}) displacements for the AP magnetic state different from those for the P magnetic state as shown in Figure 5b, which is responsible for the difference in the switching barrier between P and AP magnetic states.

3. CONCLUSIONS

In summary, we have demonstrated the magnetoelectrically coupled memristive behaviors in an MFTJ, which are induced by the coupling of the ferroelectric domain reversal and the interfacial spin state. The resistance can be continuously and reversibly tuned by varying the pulse amplitude and/or the pulse duration. Moreover, the multiple and controllable plasticity characteristic is achieved by setting P or AP magnetization alignments of electrodes, which is analogous to the plasticity form changes with morphological alterations in a biological synapse. Meanwhile, the voltage-controlled continuously tunable interfacial spin polarization is also observed to enrich the particular function of the solid-state synapse. All of the interesting phenomena could be ascribed to the interfacial magnetoelectric coupling, which is confirmed by theoretical calculations. The control of ferroelectric domain dynamics by magnetic states not only enriches our understanding of the magnetoelectric coupling fundamentally and deserves further investigations but also opens unforeseen perspective applications of magnetoelectrically coupled spintronics in next-generation neuromorphic computational architectures.

4. EXPERIMENTAL SECTION

4.1. Device Fabrication. The LSMO (~50 nm, bottom layer)/BTO/LSMO (~30 nm, top layer) heterostructures were epitaxially grown on (001)-oriented $SrTiO_3$ substrates by pulsed laser deposition (KrF laser 248 nm) at a deposition temperature of 750 °C in a flowing oxygen atmosphere of 300 mTorr. After cooling down to room temperature, a Cr/Au layer was subsequently grown by dc magnetron sputtering on the top of the multilayer for electrical contacts. The micron-scale junction in the cross-strip geometry was patterned by a three-step UV photolithography and Ar ion milling process.[24] SiO_2 deposited by radio frequency sputtering was used to isolate the bottom LSMO layer from the top Au lead. The device structure of LSMO/BTO/LSMO MFTJ is schematically shown in Figure 1b.

4.2. Characterization. The structural and chemical integrity of the cross-sectional LSMO/BTO/LSMO multilayers were characterized by atomically resolved aberration-corrected STEM and core-level EELS, which were performed on a JEOL ARM200F microscope operating at 200 kV and equipped with a probe-forming spherical-aberration corrector and Gatan image filter (Quantum 965). Room-temperature piezoresponse force microscopy (PFM) measurements of the LSMO/BTO/LSMO MFTJs were performed by an Asylum Research Cypher scanning probe microscope with conductive Pt/Ti-coated tips contacting with the top electrodes and being grounded. The PFM hysteresis loops were collected in the dual ac resonance tracking mode with triangle pulse waveforms applying on bottom electrodes.

The transport properties were characterized using a four-point probe method in a physical property measurement system (EverCool-II, Quantum Design), and the positive bias corresponds to the current flows from the top to the bottom layer. That is, a positive voltage pulse corresponds to poling the ferroelectric polarization downward. Magnetic fields (H) were applied along the [110] easy axis of the LSMO. The transport measurements of Figures 2 and 3 were performed in a 100 μm^2 MFTJ at 80 K with an electrical bias of 10 mV. The STDP curves in Figure 4 were obtained on another MFTJ with a size of 2500 μm^2 at 80 K with a bias of 10 mV. Its representative TMR and tunneling electroresistance effects are shown in Supporting Information Figure S4. To obtain the STDP curves, we always initialize the junction to an intermediate resistance state between on and off both for $\Delta t > 0$ and $\Delta t < 0$.

4.3. Theoretical Calculations. The calculations were carried out using Quantum ESPRESSO[44] with generalized gradient approximation functional. A plane-wave cutoff of 40 Ry was used in all first-principles calculations. Structural relaxations were performed using $5 \times 5 \times 1$ Monkhorst−Pack k-meshes[45] for slab models, and the atomic positions were converged until the Hellmann−Feynman forces on each atom became less than 10 meV/Å. The in-plane lattice constants of all models were fixed to the experimental lattice constant of $SrTiO_3$ (i.e., 3.905 Å) to simulate the epitaxial growth on a $SrTiO_3$ substrate. In each model, the top and bottom electrodes are separated by an 18 Å thick vacuum to avoid magnetic interaction between them. The pseudopotentials of all the atoms were generated using Vanderbilt's ultrasoft pseudopotential generation code.[46] Virtual crystal approximation is employed to introduce Sr (Ti) doping at A-site La (B-site Mn) sites, in which the pseudopotentials (U) of the virtual La_xSr_{1-x} and Mn_mTi_{1-m} ions are generated simply by compositionally averaging the pseudopotentials of Sr and La (Ti and Mn) atoms

$$U_{La_xSr_{1-x}} = xU_{La} + (1-x)U_{Sr}$$

$$U_{Mn_mTi_{1-m}} = mU_{Mn} + (1-m)U_{Ti}$$

in which x is 0.7 and m is 0.5 to simulate $La_{0.7}Sr_{0.3}Mn_{0.5}Ti_{0.5}O_3$. Because of the fact that our experiments suggested Mn diffusing into BTO barrier layers, we introduced 5% Mn at B sites to simulate $BaTi_{0.95}Mn_{0.05}O_3$.

ASSOCIATED CONTENT

Supporting Information

The Supporting Information is available free of charge on the ACS Publications website at DOI: 10.1021/acsami.7b18206.

> Ferroelectric properties, TMR and tunneling electroresistance effects, and repeatability of the resistance evolutions (PDF)

AUTHOR INFORMATION

Corresponding Authors

*E-mail: lixg@ustc.edu.cn (X.G.L.).
*E-mail: yyw@ustc.edu.cn (Y.W.Y.).
*E-mail: cgduan@clpm.ecnu.edu.cn (C.-G.D.).

ORCID

Yue-Wen Fang: 0000-0003-3674-7352
Yuewei Yin: 0000-0003-0965-4951
Xiaoguang Li: 0000-0003-4016-4483

Notes

The authors declare no competing financial interest.

ACKNOWLEDGMENTS

This work was supported by the Natural Science Foundation of China (51332007, 51622209, 51572085, 51790491, and 21521001) and the National Key Research and Development Program of China (2016YFA0300103, 2014CB921104, and 2015CB921201). The work at Penn State was supported by DOE (DE-FG02-08ER4653), and the nanofabrication of the devices was supported by NSF (DMR-1411166). The work was partially carried out at the USTC Center for Micro and Nanoscale Research and Fabrication, and the computational sources have been provided by the computing center of East China Normal University and Extreme Science and Engineering Discovery Environment (XSEDE). Y.-W.F. acknowledges David Vanderbilt and Lingling Tao for their constructive discussions on generating pseudopotentials.

REFERENCES

(1) Hebb, D. O. *The Organization of Behavior: A Neuropsychological Theory*; John Wiley and Sons, Inc.: New York, 1949.

(2) Kandel, E. R. The Molecular Biology of Memory Storage: A Dialogue Between Genes and Synapses. *Science* **2001**, *294*, 1030−1038.

(3) Burke, S. N.; Barnes, C. A. Neural plasticity in the ageing brain. *Nat. Rev. Neurosci.* **2006**, *7*, 30−40.

(4) Yang, J. J.; Strukov, D. B.; Stewart, D. R. Memristive devices for computing. *Nat. Nanotechnol.* **2013**, *8*, 13−24.

(5) Yang, Y.; Wen, J.; Guo, L.; Wan, X.; Du, P.; Feng, P.; Shi, Y.; Wan, Q. Long-Term Synaptic Plasticity Emulated in Modified Graphene Oxide Electrolyte Gated IZO-Based Thin-Film Transistors. *ACS Appl. Mater. Interfaces* **2016**, *8*, 30281−30286.

(6) Strukov, D. B.; Snider, G. S.; Stewart, D. R.; Williams, R. S. The missing memristor found. *Nature* **2008**, *453*, 80−83.

(7) Chanthbouala, A.; Matsumoto, R.; Grollier, J.; Cros, V.; Anane, A.; Fert, A.; Khvalkovskiy, A. V.; Zvezdin, K. A.; Nishimura, K.; Nagamine, Y.; Maehara, H.; Tsunekawa, K.; Fukushima, A.; Yuasa, S. Vertical-current-induced domain-wall motion in MgO-based magnetic tunnel junctions with low current densities. *Nat. Phys.* **2011**, *7*, 626−630.

(8) Lequeux, S.; Sampaio, J.; Cros, V.; Yakushiji, K.; Fukushima, A.; Matsumoto, R.; Kubota, H.; Yuasa, S.; Grollier, J. A magnetic synapse: multilevel spin-torque memristor with perpendicular anisotropy. *Sci. Rep.* **2016**, *6*, 31510.

(9) Boyn, S.; Grollier, J.; Lecerf, G.; Xu, B.; Locatelli, N.; Fusil, S.; Girod, S.; Carretero, C.; Garcia, K.; Xavier, S.; Tomas, J.; Bellaiche, L.; Bibes, M.; Barthélémy, A.; Saïghi, S.; Garcia, V. Learning through ferroelectric domain dynamics in solid-state synapses. *Nat. Commun.* **2017**, *8*, 14736.

(10) Chanthbouala, A.; Garcia, V.; Cherifi, R. O.; Bouzehouane, K.; Fusil, S.; Moya, X.; Xavier, S.; Yamada, H.; Deranlot, C.; Mathur, N. D.; Bibes, M.; Barthélémy, A.; Grollier, J. A ferroelectric memristor. *Nat. Mater.* **2012**, *11*, 860−864.

(11) Kim, D. J.; Lu, H.; Ryu, S.; Bark, C.-W.; Eom, C.-B.; Tsymbal, E. Y.; Gruverman, A. Ferroelectric tunnel memristor. *Nano Lett.* **2012**, *12*, 5697−5702.

(12) Wright, C. D.; Liu, Y.; Kohary, K. I.; Aziz, M. M.; Hicken, R. J. Arithmetic and biologically-inspired computing using phase-change materials. *Adv. Mater.* **2011**, *23*, 3408−3413.

(13) Kuzum, D.; Jeyasingh, R. G. D.; Lee, B.; Wong, H.-S. P. Nanoelectronic programmable synapses based on phase change materials for brain-inspired computing. *Nano Lett.* **2012**, *12*, 2179−2186.

(14) Zhu, L. Q.; Wan, C. J.; Guo, L. Q.; Shi, Y.; Wan, Q. Artificial synapse network on inorganic proton conductor for neuromorphic systems. *Nat. Commun.* **2014**, *5*, 3158.

(15) Balakrishna Pillai, P.; De Souza, M. M. Nanoionics-Based Three-Terminal Synaptic Device Using Zinc Oxide. *ACS Appl. Mater. Interfaces* **2017**, *9*, 1609−1618.

(16) Thomas, A.; Niehörster, S.; Fabretti, S.; Shepheard, N.; Kuschel, O.; Küpper, K.; Wollschläger, J.; Krzysteczko, P.; Chicca, E. Tunnel junction based memristors as artificial synapses. *Front. Neurosci.* **2015**, *9*, 241.

(17) Hu, W. J.; Wang, Z.; Yu, W.; Wu, T. Optically Controlled Electroresistance and Electrically Controlled Photovoltage in Ferroelectric Tunnel Junctions. *Nat. Commun.* **2016**, *7*, 10808.

(18) Wen, Z.; Li, C.; Wu, D.; Li, A.; Ming, N. Ferroelectric-Field-Effect-enhanced Electroresistance in Metal-Ferroelectric-Semiconductor Tunnel Junctions. *Nat. Mater.* **2013**, *12*, 617−621.

(19) Marrone, D. F.; Petit, T. L. The role of synaptic morphology in neural plasticity: structural interactions underlying synaptic power. *Brain Res. Rev.* **2002**, *38*, 291−308.

(20) Velev, J. P.; Duan, C.-G.; Burton, J. D.; Smogunov, A.; Niranjan, M. K.; Tosatti, E.; Jaswal, S. S.; Tsymbal, E. Y. Magnetic Tunnel Junctions with Ferroelectric Barriers Prediction of Four Resistance States from First Principles. *Nano Lett.* **2009**, *9*, 427−432.

(21) Quindeau, A.; Fina, I.; Marti, X.; Apachitei, G.; Ferrer, P.; Nicklin, C.; Pippel, E.; Hesse, D.; Alexe, M. Four-state ferroelectric spin-valve. *Sci. Rep.* **2015**, *5*, 9749.

(22) Yau, H. M.; Yan, Z. B.; Chan, N. Y.; Au, K.; Wong, C. M.; Leung, C. W.; Zhang, F. Y.; Gao, X. S.; Dai, J. Y. Low-field Switching Four-state Nonvolatile Memory Based on Multiferroic Tunnel Junctions. *Sci. Rep.* **2015**, *5*, 12826.

(23) Yin, Y.-W.; Huang, W.-C.; Liu, Y.-K.; Yang, S.-W.; Dong, S.-N.; Tao, J.; Zhu, Y.-M.; Li, Q.; Li, X.-G. Octonary Resistance States in $La_{0.7}Sr_{0.3}MnO_3/BaTiO_3/La_{0.7}Sr_{0.3}MnO_3$ Multiferroic Tunnel Junctions. *Adv. Electron. Mater.* **2015**, *1*, 1500183.

(24) Huang, W.; Lin, Y.; Yin, Y.; Feng, L.; Zhang, D.; Zhao, W.; Li, Q.; Li, X. Interfacial Ion Intermixing Effect on Four-Resistance States in $La_{0.7}Sr_{0.3}MnO_3/BaTiO_3/La_{0.7}Sr_{0.3}MnO_3$ Multiferroic Tunnel Junctions. *ACS Appl. Mater. Interfaces* **2016**, *8*, 10422−10429.

(25) Huang, W.; Yang, S.; Li, X. Multiferroic Heterostructures and Tunneling Junctions. *J. Materiomics* **2015**, *1*, 263−284.

(26) Garcia, V.; Bibes, M.; Bocher, L.; Valencia, S.; Kronast, F.; Crassous, A.; Moya, X.; Enouz-Vedrenne, S.; Gloter, A.; Imhoff, D.; Deranlot, C.; Mathur, N. D.; Fusil, S.; Bouzehouane, K.; Barthelemy, A. Ferroelectric Control of Spin Polarization. *Science* **2010**, *327*, 1106−1110.

(27) Pantel, D.; Goetze, S.; Hesse, D.; Alexe, M. Reversible Electrical Switching of Spin Polarization in Multiferroic Tunnel Junctions. *Nat. Mater.* **2012**, *11*, 289−293.

(28) Yin, Y. W.; Burton, J. D.; Kim, Y.-M.; Borisevich, A. Y.; Pennycook, S. J.; Yang, S. M.; Noh, T. W.; Gruverman, A.; Li, X. G.; Tsymbal, E. Y.; Li, Q. Enhanced Tunnelling Electroresistance Effect due to a Ferroelectrically Induced Phase Transition at a Magnetic Complex Oxide Interface. *Nat. Mater.* **2013**, *12*, 397−402.

(29) Hu, J.-M.; Duan, C.-G.; Nan, C.-W.; Chen, L.-Q. Understanding and designing magnetoelectric heterostructures guided by computation: progresses, remaining questions, and perspectives. *npj Comput. Mater.* **2017**, *3*, 18.

(30) Lee, M.-J.; Lee, C. B.; Lee, D.; Lee, S. R.; Chang, M.; Hur, J. H.; Kim, Y.-B.; Kim, C.-J.; Seo, D. H.; Seo, S.; Chung, U. I.; Yoo, I.-K.; Kim, K. A fast, high-endurance and scalable non-volatile memory device made from asymmetric $Ta_2O_{(5-x)}/TaO_{(2-x)}$ bilayer structures. *Nat. Mater.* **2011**, *10*, 625−630.

(31) Julliere, M. Tunneling Between Ferromagnetic Films. *Phys. Lett. A* **1975**, *54*, 225−226.

(32) Li, J.; Nagaraj, B.; Liang, H.; Cao, W.; Lee, C. H.; Ramesh, R. Ultrafast polarization switching in thin-film ferroelectrics. *Appl. Phys. Lett.* **2004**, *84*, 1174−1176.

(33) Tybell, T.; Paruch, P.; Giamarchi, T.; Triscone, J.-M. Domain wall creep in epitaxial ferroelectric $Pb(Zr_{0.2}Ti_{0.8})O_3$ thin films. *Phys. Rev. Lett.* **2002**, *89*, 097601.

(34) Meng, Q.; Han, M.-G.; Tao, J.; Xu, G.; Welch, D. O.; Zhu, Y. Velocity of domain-wall motion during polarization reversal in ferroelectric thin films: Beyond Merz's Law. *Phys. Rev. B: Condens. Matter Mater. Phys.* **2015**, *91*, 054104.

(35) Gao, P.; Nelson, C. T.; Jokisaari, J. R.; Baek, S.-H.; Bark, C. W.; Zhang, Y.; Wang, E.; Schlom, D. G.; Eom, C.-B.; Pan, X. Revealing the role of defects in ferroelectric switching with atomic resolution. *Nat. Commun.* **2011**, *2*, 591.

(36) Ishibashi, Y.; Takagi, Y. Note on ferroelectric domain switching. *J. Phys. Soc. Jpn.* **1971**, *31*, 506−510.

(37) Hashimoto, S.; Orihara, H.; Ishibashi, Y. Study on D-E Hysteresis Loop of TGS Based on the Avrami-Type Model. *J. Phys. Soc. Jpn.* **1994**, *63*, 1601−1610.

(38) Hu, W. J.; Juo, D.-M.; You, L.; Wang, J.; Chen, Y.-C.; Chu, Y.-H.; Wu, T. Universal ferroelectric switching dynamics of vinylidene fluoride-trifluoroethylene copolymer films. *Sci. Rep.* **2014**, *4*, 4772.

(39) Shin, Y.-H.; Grinberg, I.; Chen, I.-W.; Rappe, A. M. Nucleation and growth mechanism of ferroelectric domain-wall motion. *Nature* **2007**, *449*, 881−884.

(40) Jo, J. Y.; Han, H. S.; Yoon, J.-G.; Song, T. K.; Kim, S.-H.; Noh, T. W. Domain switching kinetics in disordered ferroelectric thin films. *Phys. Rev. Lett.* **2007**, *99*, 267602.

(41) Liu, Y.; Liang, Z.; Liu, J.; Zou, W.; Li, X.; Wang, Y.; An, L. Downregulation of caveolin-1 contributes to the synaptic plasticity deficit in the hippocampus of aged rats. *Neural Regener. Res.* **2013**, *8*, 2725−2733.

(42) Fechner, M.; Zahn, P.; Ostanin, S.; Bibes, M.; Mertig, I. Switching Magnetization by 180° with an Electric Field. *Phys. Rev. Lett.* **2012**, *108*, 197206.

(43) Baker, A. A.; Figueroa, A. I.; Pingstone, D.; Lazarov, V. K.; van der Laan, G.; Hesjedal, T. Spin pumping in magnetic trilayer structures with an MgO barrier. *Sci. Rep.* **2016**, *6*, 35582.

(44) Giannozzi, P.; Baroni, S.; Bonini, N.; Calandra, M.; Car, R.; Cavazzoni, C.; Ceresoli, D.; Chiarotti, G. L.; Cococcioni, M.; Dabo, I.; Dal Corso, A.; de Gironcoli, S.; Fabris, S.; Fratesi, G.; Gebauer, R.; Gerstmann, U.; Gougoussis, C.; Kokalj, A.; Lazzeri, M.; Martin-Samos, L.; Marzari, N.; Mauri, F.; Mazzarello, R.; Paolini, S.; Pasquarello, A.; Paulatto, L.; Sbraccia, C.; Scandolo, S.; Sclauzero, G.; Seitsonen, A. P.; Smogunov, A.; Umari, P.; Wentzcovitch, R. M. QUANTUM ESPRESSO: a modular and open-source software project for quantum simulations of materials. *J. Phys. Condens. Matter* **2009**, *21*, 395502.

(45) Monkhorst, H. J.; Pack, J. D. Special points for Brillouin-zone integrations. *Phys. Rev. B: Solid State* **1976**, *13*, 5188−5192.

(46) Vanderbilt, D. Soft self-consistent pseudopotentials in a generalized eigenvalue formalism. *Phys. Rev. B: Condens. Matter Mater. Phys.* **1990**, *41*, 7892−7895.